Wideband acoustic modulation using periodic poroelastic composite structures

Hou Qiao[a], Zeng He[a,b], Wen Jiang[a,b,*], Lin Yang[c], Weicai Peng[d]

[a]*Department of Mechanics, Huazhong University of Science & Technology, Wuhan, China*
[b]*Hubei Key Laboratory for Engineering Structural Analysis and Safety Assessment, Huazhong University of Science & Technology, Wuhan, China*
[c]*Department of Engineering Mechanics, Wuhan University of Science and Technology, Wuhan, China*
[d]*National Key Laboratory on Ship Vibration and Noise, China Ship Development and Design Center, Wuhan, China*

Abstract

We proposed an effective acoustic abatement solution comprised of periodic resonators and multi-panel structures with porous lining here, which can incorporate the wideband capability of porous materials and the low-frequency advantage of locally resonant structures together. Theoretical and numerical modeling procedures are developed using the poroelastic field with periodic boundary conditions and the synthesized resonator forces. The results obtained compare favorably with the bibliographies and the finite element models. It is found that the STL of the periodic composite structure can be tuned using proper porous additions and resonators concerning both the amplitude and the tuning bandwidth. The results reported illustrate a promising while practical alternative on low-frequency wideband sound modulation.

Keywords: Wideband acoustic modulation; poroelastic; periodic; composite structures; locally resonant structures

1. Introduction

Noise issues are frequently found in machineries used in industrial environment. Long-lasting interests are drawn on related noise abatements. However, as noise sources could be significant within a wide frequency range, their abatement and modulation are challenging.

Porous materials are recognized as wideband noise control solutions. Fruitful theoretical and numerical results on the acoustic properties of porous materials were obtained during the twentieth century [1, 2, 3, 4, 5]. As composite structures composed of porous materials, such as layered media [6] and multi-layer structures [7, 8, 9], prevail among noise control applications, research efforts on their sound transmission are remarkable. However, at low frequencies where the thermal and viscous dissipation are inefficient,

*Corresponding author
Email address: wjiang@hust.edu.cn (Wen Jiang)

porous materials are generally considered as ineffective. Recently, some researchers tries to add resonant structures into the porous matrix to improve the low-frequency performance of porous materials [10, 11]. Their results are exciting, however, the microscopic additions used are difficult to implement and their modeling procedures are too sophisticated.

Periodic structures are promising in low-frequency range due to locally resonant mechanism, which is introduced in the seminal work by Liu et al. [12]. Unlike in Bragg diffraction cases, locally resonant periodic structures can modulate elastic wave at deep subwavelength. Therefore, to obtain compact and effective low-frequency sound modulation solutions, researchers worldwide focused their interests on composite structures with periodic resonators [13, 14, 15, 16], multi-layer microperforated panel structures [17, 18], periodic Helmholtz resonators [19, 20] or combined locally resonant structures [21, 22]. Though the results reported in these bibliographies are impressive, however, locally resonant designs are always only effective in a narrow bandwidth, which is an inherent drawback. Therefore, efforts on low-frequency wideband acoustic modulation are prominent. Unfortunately, related results are scarce [13, 14, 18], to the authors' knowledge.

As periodic structures are promising in low-frequency range, while porous materials are wideband effective, the motivation here is to combine these advantages together by incorporating macroscopic locally resonant design into composite structure with porous lining. Two-dimensional periodic poroelastic composite structures, which comprise multi-panel structures with porous lining and distributed resonators, are proposed and discussed. The modeling procedures for periodically rib-stiffened composite structure with porous lining [23] is adopted and resonator forces are incorporated. The periodic problem here is finally solved by truncation, and validated by degenerated results and finite element results. By analyzing the results of the preceding periodic poroelastic composite structures, we show that low-frequency wideband acoustic modulation can be achieved.

In Section 2, the two-dimensional periodic poroelastic composite model and detailed model procedures are outlined. Subsequently, in Section 3, model validations and result discussions are provided. Section 4 ends with conclusions.

2. Two dimensional periodic poroelastic composite structure

The periodic composite structure here comprises a multi-panel structure with porous lining and distributed resonators, as shown in Fig.1-a and b. The boundary conditions between the poroelastic domain and an adjacent domain are classified using the notations in Ref.[7], i.e., B for bonded condition, O for open to an infinite air domain, and U for adjacent to but not bonded on a solid domain. The periodic resonators can be simple resonators as shown in Fig.1-c or composite resonators as shown in Fig.1-d and e (composite resonator A and B respectively). A composite structure comprises a single panel with periodic composite resonator A is shown in Fig.1-f.

A plane wave transmits through the periodic composite structure with velocity potential $\Phi_i = \mathrm{e}^{\mathrm{j}\omega t - \mathrm{j}\mathbf{kr}}$, where $\mathbf{k} = (k_x, k_z)$, $\mathbf{r} = (x, z)$, $\mathrm{j} = \sqrt{-1}$. According to Fig.1-a, $k_x = k\cos\varphi, k_z = k\sin\varphi$, here k is the incident wave number, φ is the incident elevation angle. The time dependence $\mathrm{e}^{\mathrm{j}\omega t}$ is omitted in the following. Here we make the following assumptions:

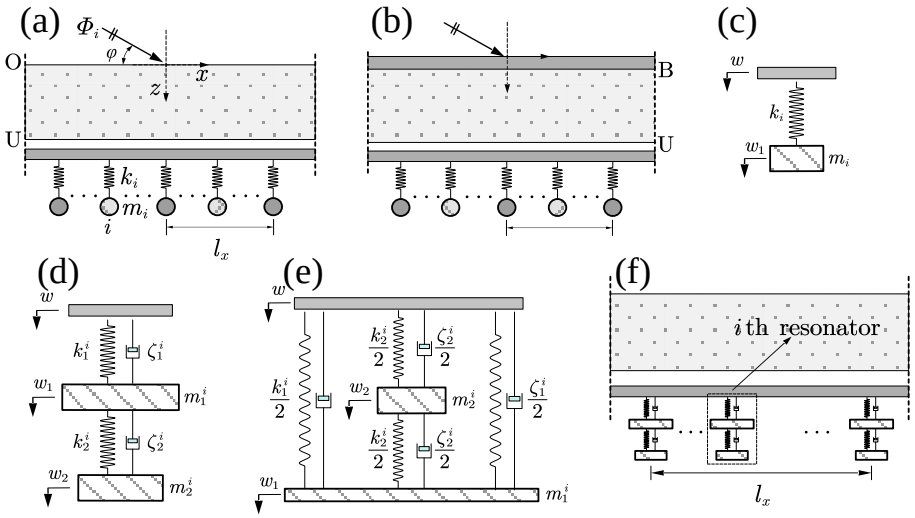

Fig. 1. Schematic diagram of the periodic composite structure. (a) A single panel composite structure with porous lining and periodic resonators (OU case, simple resonator). (b) A double panel structure with porous lining and periodic resonators (BU case, simple resonator). (c) A simple resonator. (d) Composite resonator A. (e) Composite resonator B. (f) A single panel composite structure with porous lining and periodic resonators (OU case, composite resonator A).

A1. The composite structure and its adjacent domains are all infinite, therefore no reflections from outside the composite structure is considered.

A2. The resonators are periodic along x-axis with a periodic span l_x, and multiple different resonators can be placed evenly in a periodic lattice (span).

A3. The composite structure and the resonators are ideally point-connected, therefore the resultant force of a resonator (simple resonator or composite resonator) simplifies to a concentrate force.

The above A3, however, is not substantial as distributed forces or moments can also be conveniently translated to a concentrate force and/or moment; it is provided to show the essential idea with elegance here.

2.1. Two-dimensional poroelastic domain with periodic boundary conditions

When periodic boundary conditions are present, the poroelastic displacements are assumed to comprise six groups of harmonic components [23]. According to the procedures provided in Ref.[23], the displacement $\mathbf{u} = [u_x^s, u_z^s, u_x^f, u_z^f]^T$ in the periodic poroelastic domain is obtained as

$$\mathbf{u} = \sum_m \mathrm{e}^{-\mathrm{j}k_x^m x}\ \mathbf{Y}_m \mathbf{e}_m \mathbf{C}_m \tag{1}$$

where k_x^m is the wave number component (along x-axis) of the harmonic components, u_i^s and u_i^f $(i = x, z)$ are the displacement of solid and fluid phases respectively; $\mathbf{e}_m$ and $\mathbf{C}_m$

are

$$\mathbf{e}_m = [\mathrm{e}^{\mathrm{j}k_{1z}^m z}, \mathrm{e}^{-\mathrm{j}k_{1z}^m z}, \mathrm{e}^{\mathrm{j}k_{2z}^m z}, \mathrm{e}^{-\mathrm{j}k_{2z}^m z}, \mathrm{e}^{\mathrm{j}k_{3z}^m z}, \mathrm{e}^{-\mathrm{j}k_{3z}^m z}] \tag{2}$$

$$\mathbf{C}_m = [C_1^m, C_2^m, C_3^m, C_4^m, C_5^m, C_6^m]^T \tag{3}$$

Here, $\mathrm{e}^{\pm\mathrm{j}k_{1z}^m z}, \mathrm{e}^{\pm\mathrm{j}k_{2z}^m z}$, and $\mathrm{e}^{\pm\mathrm{j}k_{3z}^m z}$ are the wave number component (along z-axis) of the harmonic components; $C_1^m (i = 1, 2 \ldots 6)$ are the unknown amplitude of the harmonic components. In Ref.[23], at normal incidence ($C_5^m = C_6^m = 0$), a numerical procedure is used to approximate the absence of wave components in $\mathbf{Y}_m$. However, in 2D case, no numerical approximation is needed and the exact closed-form expressions can be obtained. Therefore, though the derivation procedures are the same as those in Ref.[23], the non-zero elements of $\mathbf{Y}_m$ are provided in Appendix B.

Once the porous displacement $\mathbf{u}$ is obtained, the stress components in the periodic poroelastic field is [23]

$$\begin{aligned} \sigma_{ij} &= 2Ne_{ij} + (Ae_s + Qe_f)\delta_{ij} \\ s &= Qe_s + Re_f \end{aligned} \tag{4}$$

where $e_s = \partial u_x^s/\partial x + \partial u_z^s/\partial z$, $e_f = \partial u_x^f/\partial x + \partial u_z^f/\partial z$; N, A, Q, and R are poroelastic parameters detailed in Ref.[7, 23], while e_{ij} is

$$e_{ij} = \begin{cases} \partial u_i^s/\partial x_i, & i = j \\ \frac{1}{2}\left(\partial u_i^s/\partial x_j + \partial u_j^s/\partial x_i\right), & i \neq j \end{cases}, \quad \delta_{ij} = \begin{cases} 1, & i = j \\ 0, & i \neq j \end{cases}$$

Here x_i and x_j denote x or z coordinate; in other variables, i, j denote x or z.

2.2. In-plane and transverse vibration of the plates

As the frequency range discussed is far below the coincidence frequency of the plate here, the thin plate theory is used; otherwise, the Timoshenko-Mindlin plate theory should be used. Therefore, in the periodic poroelastic composite structure here, when in-plane and out-of-plane force or moment is present, the vibration equations of the plate are [23]

$$\mathcal{L}_i(u) = f_x, \quad \mathcal{L}_t(w) = f_z + \frac{\partial \mathcal{M}_y}{\partial x} \tag{5}$$

where

$$\mathcal{L}_i(u) = \rho_p h \frac{\partial^2 u}{\partial t^2} - D_p \frac{\partial}{\partial x}\left(\frac{\partial u}{\partial x}\right), \; \mathcal{L}_t(w) = D\nabla^4 w + \rho_p h \frac{\partial^2 w}{\partial t^2}$$

Here, $\mathcal{L}_i(\cdot)$ and $\mathcal{L}_t(\cdot)$ are the in-plane and out-of-plane vibration operator, u and w are the in-plane and out-of-plane displacements, f_x and f_z are the in-plane and out-of-plane forces, $\mathcal{M}_y$ is the in-plane moment normal to the $x - z$ plane; ρ_p, h, D_p, and D are the density, thickness, in-plane stiffness, and the transverse stiffness of the plate.

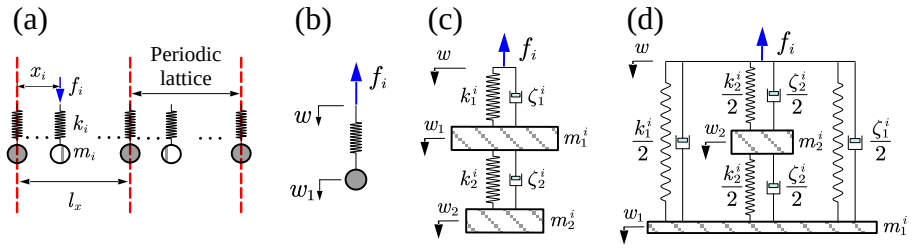

Fig. 2. Schematic diagram of the distribution of the spring force. (a) The spring force distribution in a periodic lattice. (b) The displacements and resultant force in a simple resonator. (c-d) The displacements and resultant force in composite resonator A and B respectively.

2.3. Periodic resonators and their resultant forces

According to the assumptions A2 and A3, the schematic diagram of the spring forces (simple resonators) is shown in Fig.2-a; the total number of resonators in a periodic lattice is denoted as N_s, and the resonator i ($i = 1, 2 \dots N_s$) is located at x_i in the periodic span.

According to Fig.2-b, we can get the force f_i of a simple resonator i as following

$$f_i = \frac{m_i \omega^2}{1 - \omega^2/[\omega_i^2(1 + \mathrm{j}\eta_i)]} w \tag{6}$$

where w is the displacement of the plate which the resonators are attached to; $\omega_i = \sqrt{k_i/m_i}$ is the natural circular frequency of the resonator i, m_i is its mass, k_i is its spring stiffness, η_i is the spring damping [13].

Meanwhile, according to Fig.2-c and d, the force f_i of a composite resonator i (composite resonator A or B) is

$$f_i = X_3 \cdot w \tag{7}$$

where $\mathbf{X} = [X_1, X_2, X_3]^T = \mathbf{HF}$, $\mathbf{H} = (\mathbf{K} + \mathrm{j}\omega\mathbf{C} - \omega^2\mathbf{M})^{-1}$; the matrices $\mathbf{K}, \mathbf{C}, \mathbf{M}$, and $\mathbf{F}$ of composite resonator A or B can all be got by their dynamic equations [16]. Their elements are provided in Appendix A.

Therefore, the resultant force F_{sum} of the periodic resonators is

$$F_{\mathrm{sum}} = \sum_n \sum_i \beta_i f_i \delta(x - n l_x - x_i) \tag{8}$$

Here, x_i is the position of resonator i, $x_i = ia$, a is the distance between two adjacent resonators; integer $n = -\infty, \dots + \infty$, integer $i = 0, 1, \dots N_s$,

$$\delta(x) = \begin{cases} 1 & x = 0 \\ 0 & x \neq 0 \end{cases}, \quad \beta_i = \begin{cases} 1 & q = 1, \dots (N_s - 1) \\ 1/2 & q = 0 \text{ or } N_s \end{cases} \tag{9}$$

β_i is the contribution coefficient of a resonator to lattice n.

2.4. The acoustic domain and BC conditions

According to the boundary conditions of the periodic composite structure, there exists one incident acoustic domain, one transmitted acoustic domain, and one or more intermediate acoustic layers between the porous domain and the multi-panel structure. The acoustic domains are all assumed linear, and the related velocity potential Φ follows

$$\nabla^2\Phi - \frac{1}{c^2}\frac{\partial^2\Phi}{\partial t^2} = 0 \tag{10}$$

where c is the corresponding sound velocity.

The boundary conditions between the porous domain and the multi-panel structure were detailed before [7, 8, 24], therefore, the details are not provided here. However, different coordinate frames may be used, and the boundary conditions can be different [23]. Attentions should be paid to the coordinate frame used and the related boundary conditions.

2.5. The harmonic expansions and system equations

The periodic composite structure comprises acoustic domains, porous domains, multi-panel structures, and periodic resonators. To show the essential ideas with an elegant formulation, we limit the multi-panel structure to a single panel or a double panel here. The boundary conditions can be OU/OB for the single panel cases (Fig.3-a and b), and BB/BU/UU for the double panel cases (Fig.3-c, d and e).

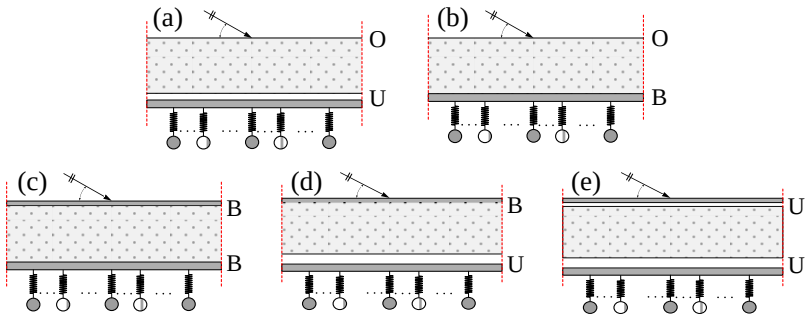

Fig. 3. Schematic diagram of different boundary conditions (simple resonators can be replaced by composite resonators): (a-b) single panel case, OU and OB boundary conditions respectively; (c-e) double panel case, BB, BU, and UU boundary conditions respectively.

In the following, we use OU case as an example to show the system equations and the solution procedures. In OU case, the periodic composite structure comprises an incident acoustic domain, a porous domain, an intermediate acoustic domain, a plate, and a transmitted acoustic domain (Fig.1-a).

According to the law of refraction and the method of space harmonic series (SHS),

the velocity potential of the three acoustic domains can be expressed as

$$\Phi_1 = \mathrm{e}^{-\mathrm{j}(k_x x + k_z z)} + \sum_m R_1^m \mathrm{e}^{-\mathrm{j}\left(k_x^m x - k_{z,i}^m z\right)} \tag{11}$$

$$\Phi_2 = \sum_m I_2^m \mathrm{e}^{-\mathrm{j}\left(k_x^m x - k_{z,a}^m z\right)} + \sum_m R_2^m \mathrm{e}^{-\mathrm{j}\left(k_x^m x - k_{z,a}^m z\right)} \tag{12}$$

$$\Phi_3 = \sum_m T_3^m \mathrm{e}^{-\mathrm{j}\left(k_x^m x - k_{z,t}^m z\right)} \tag{13}$$

where $k_{z,i}^m, k_{z,a}^m$, and $k_{z,t}^m$ are the the wave number component (along z-axis) of the harmonic components; R_1^m, I_2^m, R_2^m, and T_3^m are the amplitude of the wave harmonics which can be solved by the boundary conditions. $k_{z,i}^m, k_{z,a}^m$, and $k_{z,t}^m$ can be solved by substituting Eq.(11), (12), and (13) into Eq.(10)

$$k_{z,\times}^m = \sqrt{k^2 - (k_x^m)^2}, k = \omega / c_\times \quad (\times = i, a, \text{or } t) \tag{14}$$

Here $c_\times$ is the sound velocity in the corresponding domain.

In the thin plate, according to the law of refraction and the method of space harmonic series (SHS), the displacement $\mathbf{u} = [u, w]^T$ expands to

$$\mathbf{u} = \sum_m \mathbf{U}^m \mathrm{e}^{-\mathrm{j}k_x^m x} \tag{15}$$

where $\mathbf{U}^m = [U^m, W^m]^T$ is the unknown component amplitude vector. In OU case, the in-plane displacement u is absent, therefore, only amplitude W^m is included.

In OU case, all the boundary conditions at the interfaces of different domains or at the middle plane are

$$\begin{gathered}
\text{(i)} - \epsilon\rho_i \frac{\partial \Phi_1}{\partial t} - s = 0 \quad \text{(ii)} - (1-\epsilon)\rho_i \frac{\partial \Phi_1}{\partial t} - \sigma_z = 0 \\
\text{(iii)}(1-\epsilon)\frac{\partial u_z^s}{\partial t} + \epsilon \frac{\partial u_z^f}{\partial t} = -\frac{\partial \Phi_1}{\partial z} \quad \text{(iv)}\tau_{zx} = 0 \\
\text{(v)} - \epsilon\rho_a \frac{\partial \Phi_2}{\partial t} - s = 0 \quad \text{(vi)} - (1-\epsilon)\rho_a \frac{\partial \Phi_2}{\partial t} - \sigma_z = 0 \\
\text{(vii)}(1-\epsilon)\frac{\partial u_z^s}{\partial t} + \epsilon \frac{\partial u_z^f}{\partial t} = -\frac{\partial \Phi_2}{\partial z} \quad \text{(viii)}\tau_{zx} = 0 \\
\text{(ix)}\frac{\partial w}{\partial t} = -\frac{\partial \Phi_2}{\partial z} \\
\text{(x)} D\frac{\partial^4 w}{\partial x^4} + \rho_p h \frac{\partial^2 w}{\partial t^2} = \rho_a \frac{\partial \Phi_2}{\partial t} - \rho_t \frac{\partial \Phi_3}{\partial t} + \sum_n \sum_i \beta_i f_i \delta(x - n l_x - x_i) \\
\text{(xi)}\frac{\partial w}{\partial t} = -\frac{\partial \Phi_3}{\partial z}
\end{gathered} \tag{16}$$

where $\rho_\times$ is the density of the related domain; ϵ is the porosity of the porous media; σ_z, τ_{zx}, and s are the normal stress, shear stress and fluid pressure of the solid and fluid phases in the porous media respectively, and they can be got using Eq.(4).

2.6. The solution procedures (OU case)

In Eq.(16).(x), double or triple summation occurs; therefore, the resonator force term is rearranged. The cumbersome rearrangement procedures are provided in Appendix C.

Subsequently, according to the orthogonal property below

$$\int_{-l_x/2}^{l_x/2} \mathrm{e}^{-\mathrm{j}k_x^m x} \mathrm{e}^{\mathrm{j}k_x^p x} \mathrm{d}x = \begin{cases} l_x, & m = p \\ 0, & m \neq p \end{cases} \tag{17}$$

where integer $m, p = -\infty, \ldots + \infty$; Equation (16) becomes

$$\mathbf{A}_m \mathbf{x}_m = \sum_n \mathbf{B}_n \mathbf{x}_n + \mathbf{p} \tag{18}$$

where

$$\mathbf{x}_m = [C_1^m, C_2^m, C_3^m, C_4^m, C_5^m, C_6^m, W^m, R_1^m, I_2^m, I_2^m, T_3^m]^T \tag{19}$$

Integer $m, n = -\infty, \ldots + \infty$; $\mathbf{A}_m, \mathbf{B}_n$ and $\mathbf{p}$ are provided in Appendix E. To obtain a numerical solution, the preceding equation Eq.(18) is rearranged using

$$\tilde{\mathbf{x}} = [\cdots,\ \mathbf{x}_{m-1}^T,\ \mathbf{x}_m^T,\ \mathbf{x}_{m+1}^T,\ \cdots]^T \tag{20}$$

$$\tilde{\mathbf{A}} = \begin{bmatrix} \ddots & & & & & \\ & \mathbf{A}_{m-1} & & & & \\ & & \mathbf{A}_m & & & \\ & & & \mathbf{A}_{m+1} & & \\ & & & & \ddots & \end{bmatrix} \tag{21}$$

$$\tilde{\mathbf{B}} = \begin{bmatrix} & & \vdots & & \\ \cdots & \mathbf{B}_{n-1} & \mathbf{B}_n & \mathbf{B}_{n+1} & \cdots \\ \cdots & \mathbf{B}_{n-1} & \mathbf{B}_n & \mathbf{B}_{n+1} & \cdots \\ \cdots & \mathbf{B}_{n-1} & \mathbf{B}_n & \mathbf{B}_{n+1} & \cdots \\ & & \vdots & & \end{bmatrix} \tag{22}$$

$$\tilde{\mathbf{p}} = [\cdots,\ \mathbf{0}^T,\ \mathbf{p}^T,\ \mathbf{0}^T,\ \cdots]^T \tag{23}$$

Here, the blank blocks of $\tilde{\mathbf{A}}$ are all zero, while $\tilde{\mathbf{B}}$ is a full block matrix; $\mathbf{0}^T$ is a zero 1×14 vector. Subsequently, Eq.(18) becomes

$$(\tilde{\mathbf{A}} - \tilde{\mathbf{B}})\tilde{\mathbf{x}} = \tilde{\mathbf{p}} \tag{24}$$

As the dimension of matrices $\tilde{\mathbf{A}}, \tilde{\mathbf{B}}$, and vectors $\tilde{\mathbf{x}}$, $\tilde{\mathbf{p}}$ are all infinite, Equation (24) is an infinite matrix equation, which should be truncated to solve. We will detail the truncation procedures in the following. When m is truncated to $[-\hat{m}, \hat{m}]$, $\tilde{\mathbf{A}}$ and $\tilde{\mathbf{B}}$ are truncated to $14\hat{M} \times 14\hat{M}$ matrices $\bar{\mathbf{A}}$ and $\bar{\mathbf{B}}$, vectors $\tilde{\mathbf{x}}$ and $\tilde{\mathbf{p}}$ as $14\hat{M} \times 1$ vectors $\bar{\mathbf{x}}$ and $\bar{\mathbf{p}}$, $\hat{M} = 2\hat{m} + 1$; therefore, Equation (24) is solved

$$\bar{\mathbf{x}} = (\bar{\mathbf{A}} - \bar{\mathbf{B}})^{-1}\bar{\mathbf{p}} \tag{25}$$

Subsequently, the unknown amplitude of the harmonic components are determined.

The sound transmission coefficient τ of the composite structure is [23, 25]

$$\tau(\varphi) = \frac{\rho_t}{\rho_i} \frac{\sum_m |T_3^m|^2 \mathrm{Re}(k_{z,t}^m)}{\mathrm{Re}(k_z)} \tag{26}$$

Here Re$(\cdot)$ is the real operator for a complex variable. When sound wave transmit through the composite structure at $\varphi \in [\varphi_{\text{lim}}, \pi/2]$, where φ_{lim} is the minimum elevation angle (that sound can transmit), the sound transmission loss (STL) of the preceding composite structure is defined as

$$\text{STL} = 10\log(1/\bar{\tau}),\ \bar{\tau} = \frac{\int_{\varphi_{\text{lim}}}^{\pi/2} \tau(\varphi)\sin\varphi\cos\varphi\ \mathrm{d}\varphi}{\int_{\varphi_{\text{lim}}}^{\pi/2} \sin\varphi\cos\varphi\ \mathrm{d}\varphi} \tag{27}$$

When the unknown velocity amplitudes are obtained, STL can be solved by numerical integration subsequently.

3. Results and discussions

The convergence characteristics of the periodic poroelastic composite structure are complicated [23], therefore, a convergence check step, which is confirmed as reliable and accurate [26, 25, 23], is performed before any further computations to determine the appropriate $\hat{m}$. The convergence criteria is chosen as ΔSTL = 0.1dB at f_{max}=10kHz, i.e., when the variation in STL by changing $\hat{m}$ (add or minus by one) is less than 0.1dB, it is considered as converged.

Table 1
Model parameters: air gap thickness h_a = 2 mm for the OU case; h_a = 14 mm for the BU case; h_{a1} = 2mm, h_{a2} = 6 mm for the two air gaps in the UU case; $l_x = h_p, (h_p + h_a), h_p, (h_p + h_a)$, and $(h_p + h_{a1} + h_{a2})$ for the OB, OU, BB, BU, and UU cases, respectively; the gap properties $\rho_g = \rho_i, c_g = c_i$ and the transmitted side media properties $\rho_t = \rho_i, c_t = c_i$

Parameters	Descriptions	Value
Acoustic media		
ρ_i	density (incident side)	1.205 kg/m^3
c_i	sound velocity (incident side)	343 m/s
Panels		
h_1	panel thickness (incident/single panel)	1.270 mm
h_2	panel thickness (transmitted)	0.762 mm
ρ_p	density of face panels	2700 kg/m^3
E_p	Young's modulus of face panels	70×10^9Pa
ν_p	Poisson's ratio of face panels	0.33
Porous media		
ρ_s	bulk density of solid phase	30 kg/m^3
ρ_f	density of fluid phase	1.205 kg/m^3
E_s	Young's modulus (solid phase)	8×10^5Pa
ν_s	Poisson's ratio (solid phase)	0.4
η_s	loss factor (solid phase)	0.265
ϵ	the porosity	0.9
ϵ'	the tortuosity	7.8
σ	flow resistivity	2.5×10^4 MKS Rayls/m
h_p	thickness of porous core	27 mm

The parameter values are provided in Table 1 and used if not specified again. The STL is calculated in 1/24 octave bands between 10Hz and 10kHz using Simpson's Rule; the

integration domain is split into 90 subdivisions. In 2D case, different minimum elevation angle φ_{lim} are used [7, 13, 25], either by experiment data or theoretical prediction. To comply with the bibliographies, in the single panel case here φ_{lim} is 0 [13, 25], while for the double panel case, φ_{lim} is $\pi/10$ [7]. As STL is sensitive to the total mass [27], here the mass ratio γ of the resonators, i.e. the percentage of the resonator mass in the total mass, is kept constant as $\gamma = 0.2$ [13, 16] in the following.

The results of the five different boundary conditions here are fruitful, however, only some essential thus important results are provided (otherwise given in the supplementary materials) to report the findings concisely.

3.1. Model validations

To validate the preceding periodic composite model and show the wideband applicability, firstly, the results obtained are compared with the low-frequency results reported before by degenerated models and those obtained by FEM; secondly, comparisons with high-frequency results are also reported. The FEM model numerical setups are not detailed here as they are identical to those in Ref.[23] except that it is 2D here.

3.1.1. Low-frequency validations

In the low-frequency range, comparisons with the multiple identical simple resonator (resonance frequency f_r=300Hz) or composite resonator (resonance frequency f_1^0=300Hz) results in Ref.[13, 16] are made.

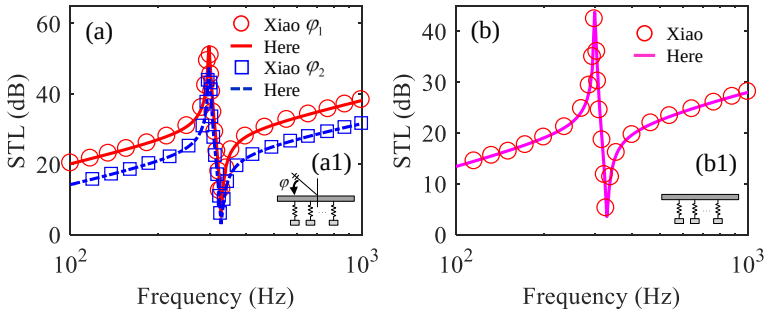

Fig. 4. Comparison of predictions (lines) versus Ref. [13] (symbols) (a) oblique incidence case $\varphi_1 = \pi/2$ or $\varphi_2 = \pi/6$ and (b) random incidence case, (a1) and (b1) are the schematic diagram respectively. The frequency range studied is [100Hz, 1kHz].

As shown in Fig.4 and 5, either the oblique incidence case results (Fig.4-a) or the random incidence case results (Fig.4-b and Fig.5-a to f) all show excellent consistency.

Some of the oblique incidence FEM results are shown in Fig.6 (OB, BB, and UU cases). As shown, the overall consistency is satisfactory. The results in Fig.4, Fig.5, and Fig.6 confirmed the validity here in the low-frequency range.

3.1.2. High-frequency validations

In the high-frequency range, result comparisons versus Ref.[13] and FEM are presented (the resonance frequency f_r or f_1^0 is 3kHz if not specified).

Comparisons versus Ref.[13] are shown in Fig.7. As shown, the overall consistency is satisfactory.

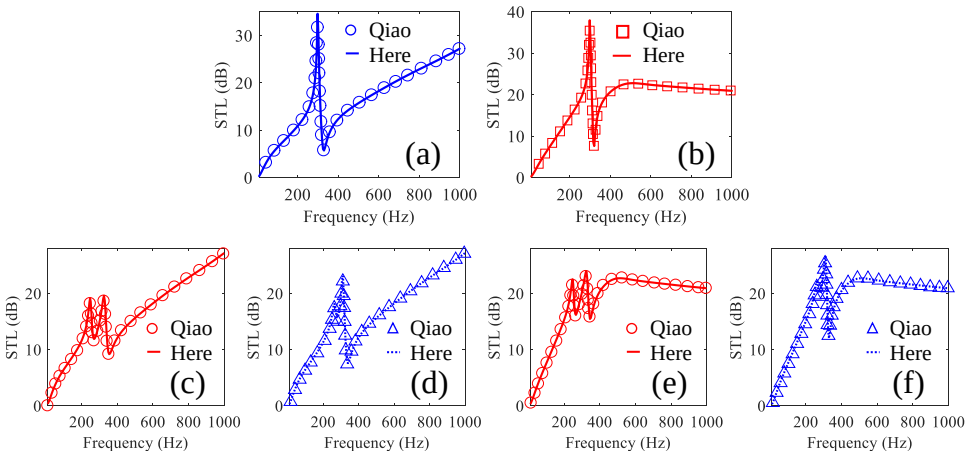

Fig. 5. Comparison of predictions (lines) versus Ref. [16] (symbols): (a-b) multiple simple resonators, OU and OB respectively; (c-d) multiple composite resonator A or B, OU case; (e-f) multiple composite resonator A or B, OB case. The frequency range studied is [10Hz, 1kHz].

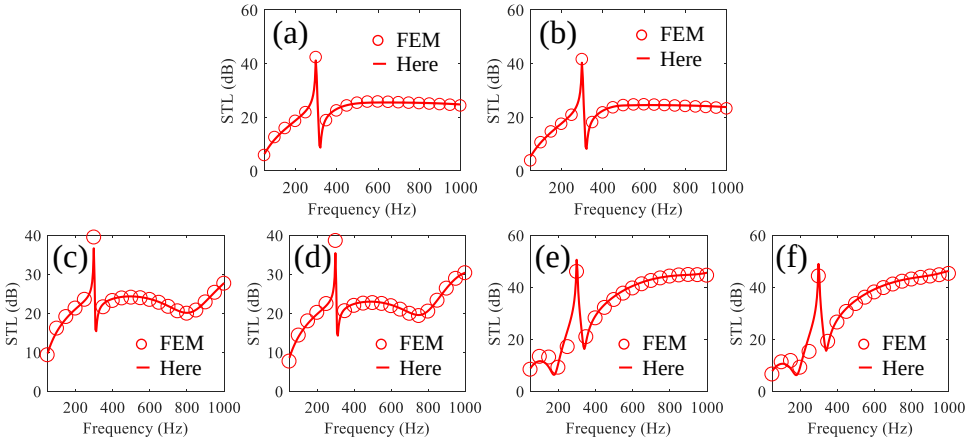

Fig. 6. Comparison of predictions (lines) versus FEM results (symbols): (a-b) OB case, $\varphi = \pi/2, \pi/3$ respectively; (c-d) BB case, $\varphi = \pi/2, \pi/3$ respectively; (e-f) UU case, $\varphi = \pi/4, \pi/6$ respectively. The frequency range studied is [10Hz, 1kHz].

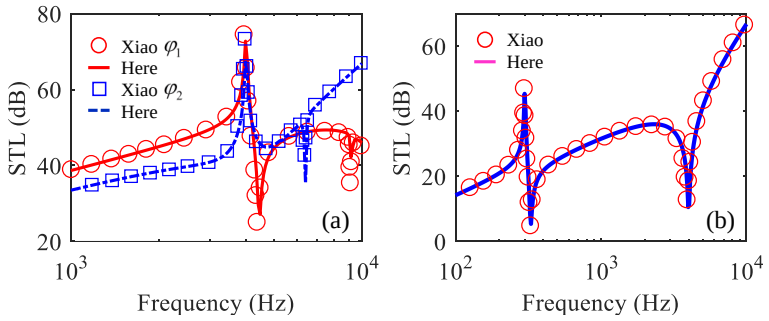

Fig. 7. Comparison of predictions (lines) versus Ref. [13] (symbols) (a) oblique incidence case $\varphi_1 = \pi/3$ or $\varphi_2 = \pi/6$, f_r=4kHz; (b) random incidence case, f_r=300Hz. The frequency range studied is [1kHz, 10kHz] and [100Hz, 10kHz] respectively.

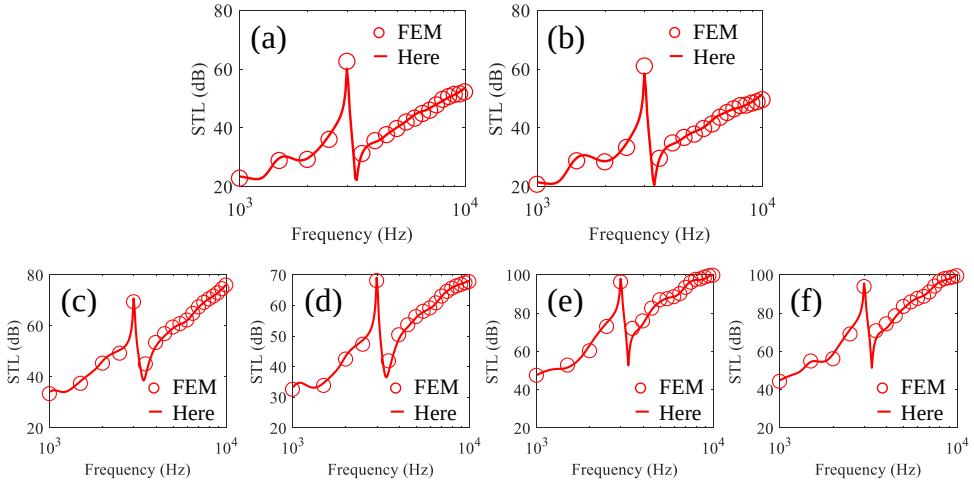

Fig. 8. Comparison of predictions (lines) versus FEM results (symbols): (a-b) OB case, $\varphi = \pi/4, \pi/6$ respectively; (c-d) BB case, $\varphi = \pi/4, \pi/6$ respectively; (e-f) BU case, $\varphi = \pi/2, \pi/3$ respectively. The frequency range studied is [1kHz, 10kHz].

Some oblique incidence result comparisons versus FEM results are shown in Fig.8 (OB, BB, and BU cases). As shown, the results here compare favorably with FEM results. The results in Fig.7 and Fig.8 confirmed the validity here in the high-frequency range.

The wideband applicability of the preceding theoretical and numerical periodic composite structure models are confirmed by Fig.4 to Fig.8.

3.2. Influence of porous additions on the STL

To show the influence of porous additions, here we used multiple identical simple resonators in a periodic span, where m_i=27g, η_i=0.01. Fig.9 (OU and OB cases) shows the comparisons between the STL of the periodic composite structures (porous + resonator,

f_r=3kHz), multi-panel structures (porous), and plate with periodic simple resonators (metamaterial plate, f_r=3kHz).

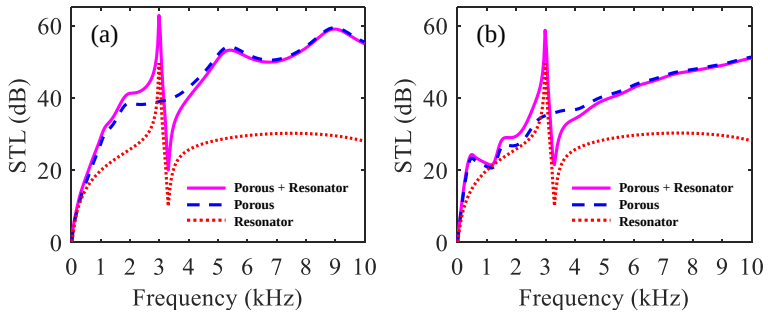

Fig. 9. Influence of porous additions on the STL (a) OU case and (b) OB case.

From Fig.9, we can see porous additions can improve the STL of the periodic composite structure away from the resonance frequency, and ease the the STL decrease around the local resonance. As porous media has wideband attenuation capability, its wideband improvement is conceivable; meanwhile, around the resonance frequency, its can attenuate the sound transmission even though resonance is prominent. In summary, the STL of the periodic composite structure can be considered as the superposition of contributions from porous additions and simple resonators separately.

3.3. Influence of identical simple resonators on the STL

Fig.10 shows the results of the periodic composite structure here with multiple identical simple resonators (different resonance frequencies respectively) under different boundary conditions (OB, OU, BB and BU cases). Here m_i=27g, η_i=0.01.

As shown, notable STL improvement occur around the resonance frequency f_r (a local crest), with a decrease around the subsequent anti-resonance frequencies (a local trough). The overall STL recovers to the cases without resonators (the solid lines in Fig.10) away from the resonance frequencies. However, as f_r increases, the improvement around the resonance frequency weakens (Fig.10-a and c f=8kHz, Fig.10-b and d f=7, 8kHz); the STL shows multiple troughs subsequently. The extra troughs are because of the coupling between resonators and the corresponding composite structures. Quantitative analyses on the dispersion relations are in progress.

3.4. Influence of identical composite resonators on the STL

Composite (multiple-degree-of-freedom) resonators can provide better vibration or wave attenuation [15]. Therefore, two composite resonator cases (Fig.1-d and e) are used here to evaluate the sound insulation performance. In composite resonator i, we denote $m_2^i = r \cdot m_1^i$, $k_2^i = s \cdot k_1^i$, $\zeta_2^i = t \cdot \zeta_1^i$, and the damping ratio $\eta_n^i = \zeta_n^i / 2m_n^i\omega_n^i$, $\omega_n^i = \sqrt{k_n^i/m_n^i}$ (n=1, 2 for the primary and secondary resonators respectively). If no damping is present (i.e. $\zeta_1^i = \zeta_2^i = 0$), the resonance frequencies of composite resonator A are [15, 16]

$$f_{1,2} = \frac{\omega_1^i}{2\pi}\sqrt{\frac{r+s+rs \pm \sqrt{(r+s+rs)^2 - 4rs}}{2r}} \tag{28}$$

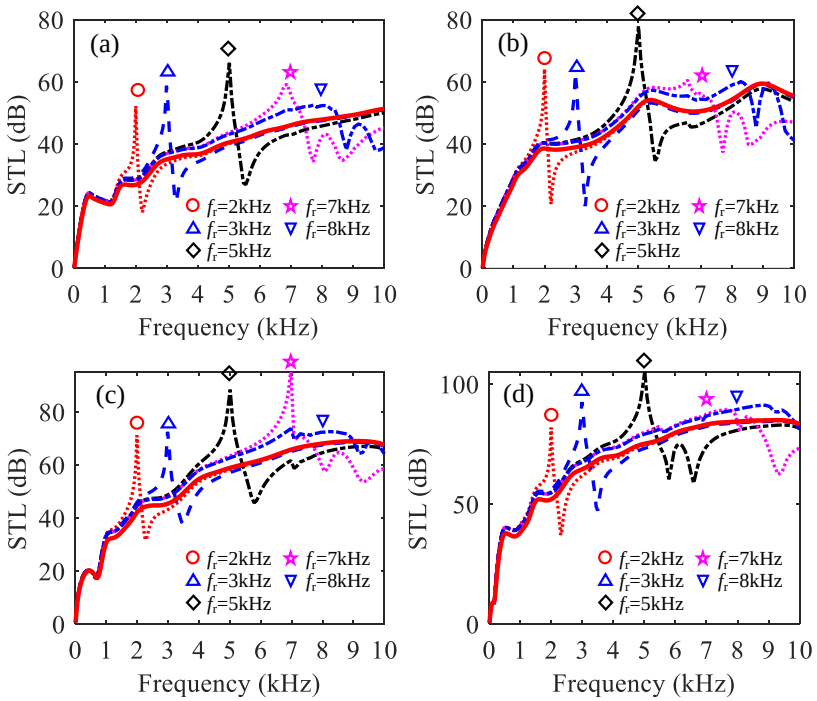

Fig. 10. Influence of identical simple resonators on the STL (a) OB case, (b) OU case, (c) BB case, and (d) BU case. Different lines (markers) correspond to different resonance frequency cases; the solid lines show the results without resonators.

The resonance frequencies of composite resonator B are [16]

$$f_{1,2} = \frac{\omega_1^i}{2\pi}\sqrt{\frac{2r+2s+rs \pm \sqrt{(2r-2s+rs)^2+4rs^2}}{4r}} \tag{29}$$

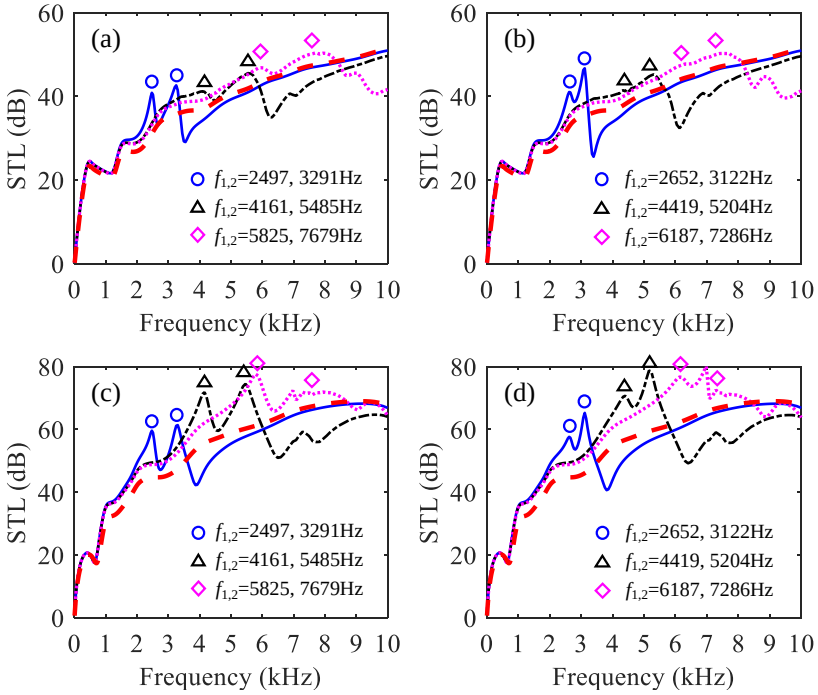

Fig. 11. Influence of identical composite resonators on the STL (a-b) OB case (composite A and B respectively) and (c-d) BB case (composite A and B respectively). Different lines (markers) correspond to different resonance frequency cases; the thick dashed lines (unmarked) show the results without resonators.

Fig.11 shows the results of the periodic composite structures here with multiple identical composite resonators (A or B, with different resonance frequencies) under different boundary conditions (OB and BB cases). Parameter values in Table 2 are used.

Table 2
Parameters of the composite resonators.

Parameters	γ	m_1^i	r	s	η_1^i	η_2^i
Values	0.2	30 g	0.0750	0.0625	0.01	0.05

As shown, notable STL improvements occur around the resonance frequencies $f_{1,2}$ (local crests), with decreases around the subsequent anti-resonance frequencies (local troughs). The overall STL recovers to the cases without resonators (the thick dashed lines in Fig.11) away from the resonance frequencies. However, as $f_{1,2}$ increases, the

improvement around the resonance frequency weakens; additional STL troughs emerge subsequently. The extra troughs are analogous to the cases with multiple identical simple resonators.

3.5. Influence of multiple simple resonators on the STL

Table 3
Parameters of multiple simple resonator cases I and II, the mass ratio γ=0.2; for resonator i, the mass m_i and resonance frequency f_r^i are $m_i = m_0 + (i-1)\Delta m$, $f_r^i = 3 + 0.5(i-1)$(kHz), $i = 1, \ldots N_s$, N_s=4,... 7.

Case	Description	m_0	Δm	η_i
I	Constant m_i	m_{sum}/N_s	0	0.05
II	Increasing m_i	$m_{\text{sum}}/N_s - (N_s-1)\Delta m/2$	$0.04m_{\text{sum}}$	0.05

Two multiple simple resonator cases are investigated here using the parameters in Table 3. The STL results of the periodic composite structures are shown in Fig.12 (OB and BU boundary conditions, case I and II respectively).

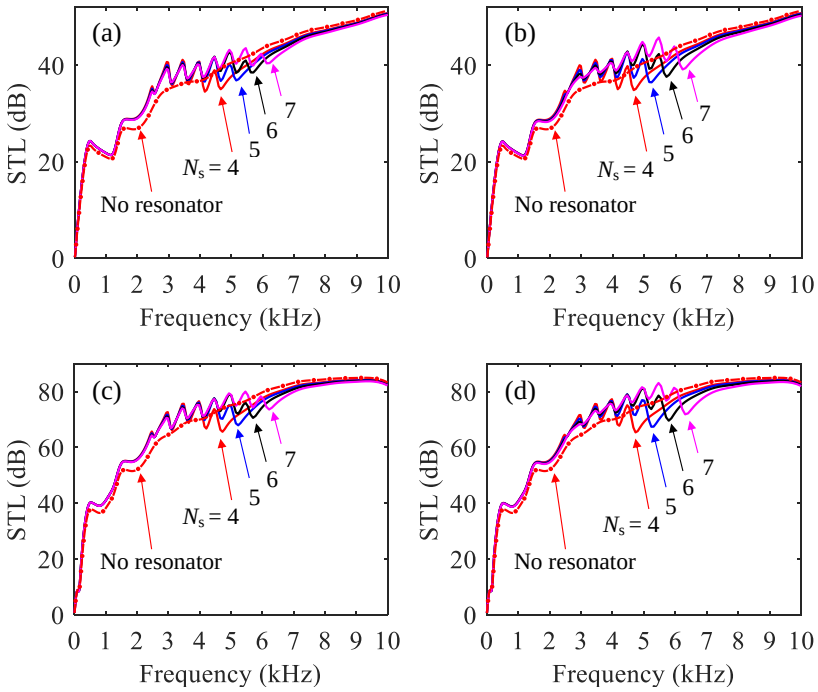

Fig. 12. Influence of multiple simple resonators on the STL (a-b) OB case (case I and II respectively) and (c-d) BU case (case I and II respectively).

As shown, the STL can be tuned around the resonance frequencies of the simple resonators. When the resonance frequencies are in the low-frequency range, the sound insulation of the periodic composite structure can be improved; however, as the resonance

frequencies increase, the sound insulation deteriorates and becomes not better than the cases without resonators. As the resonator number N_s increases, the STL amplitude and its modulation bandwidth can be tuned in either case I or II. Furthermore, while cases I and II are analogous, their STL are slightly different. A comparison is made in the following.

The local STL crests and troughs are caused by the resonance and anti-resonance of the periodic resonators. The extremum amplitudes and bandwidths are determined by the damping and resonance frequencies of the resonators. If multiple simple resonators are properly selected, the STL amplitudes and the bandwidths can be tuned, therefore, the sound insulation performance here are modulated.

3.6. Influence of multiple composite resonators on the STL

Composite resonators with different resonance frequencies are arranged in a single lattice using parameters in Table 4; in resonator i, the resonance frequency of the primary mass is chosen as $f_1^i = f_1^0 + 500(i-1)$(Hz), $i = 1, \ldots N_s$. The results are shown in Fig.13 (BB and BU boundary conditions, multiple composite resonator A or B cases respectively).

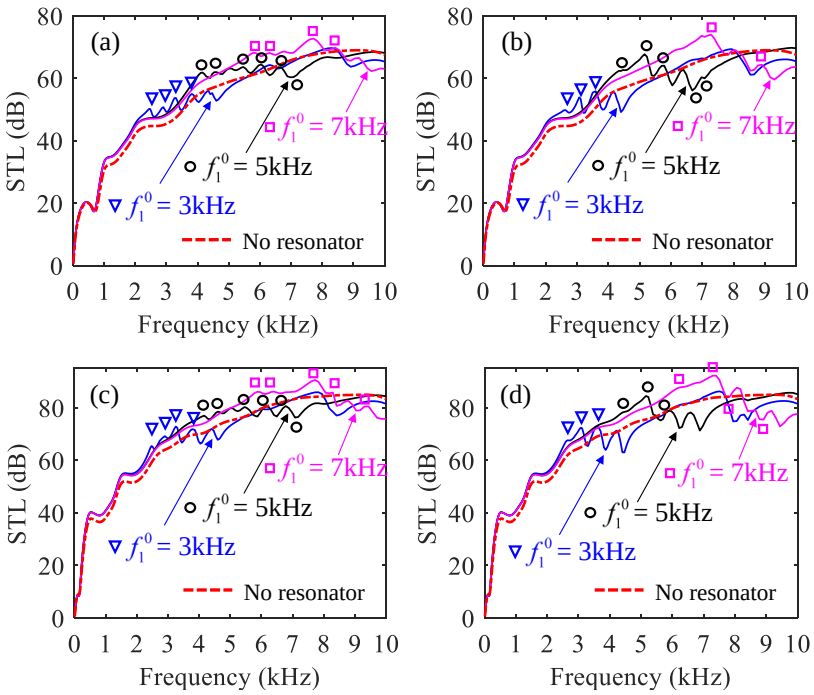

Fig. 13. Influence of multiple composite resonators on the STL (a-b) BB case (different composite resonator A and B cases respectively) and (c-d) BU case (different composite resonator A and B cases respectively). The markers show the resonance frequencies (partial, clearly identifiable ones) in the corresponding cases, and the arrows differentiate resonator cases.

Apart from the resonance frequencies obtained by Eq.(28) and (29), when damping is included, the characteristic frequencies of composite resonators (A or B) can be

Table 4
Parameters of the composite resonators

Parameters	γ	N_s	r	s	η_1^i	η_2^i
Values	0.2	4	0.0750	0.0625	0.01	0.05

determined by a quartic equation

$$A_4\omega^4 + A_3\omega^3 + A_2\omega^2 + A_1\omega + A_0 = 0 \tag{30}$$

For composite resonator A, the coefficients are $A_4 = r$, $A_3 = -2\mathrm{j}(r + t + rt)\eta_1\omega_1$, $A_2 = -(r + s + rs + 4t\eta_1^2)\omega_1^2$, $A_1 = 2\mathrm{j}(s + t)\eta_1\omega_1^3$, and $A_0 = s\omega_1^4$; as to composite resonator B, $A_4 = r$, $A_3 = -\mathrm{j}(2r + 2t + rt)\eta_1\omega_1$, $A_2 = -\left[r + s + \frac{1}{2}rs + (4t + t^2)\eta_1^2\right]\omega_1^2$, $A_1 = \mathrm{j}(2s + 2t + st)\eta_1\omega_1^3$, and $A_0 = \frac{1}{4}\left(4s + s^2\right)\omega_1^4$. The characteristic frequencies are determined by solving these quartic equations.

As shown in Fig.13, the STL can be improved around the resonance frequencies in the low-frequency range; however, as the resonance frequencies increase, the STL deteriorates and becomes not better than the cases without resonators. This is analogous to the cases of simple resonators. Furthermore, the influence of the lower resonance frequencies are noteworthy compared to the higher ones; in addition, the influence of the latter tends to vanish, and distinct STL troughs can even be seen because of complex coupling between the resonators and the structures. Quantitative analyses are in progress at the moment.

3.7. Comparison between different resonator cases

To show the differences between the above four resonator cases, we choose N_s=4, γ=0.2 (other parameters as those in Table 3 and 4), and the resonance frequencies (f_r^i or f_1^i) as $3000 + 500(i - 1)$(Hz), $i = 1, \ldots N_s$, and provide all the results in Fig.14.

As shown in Fig.14, the bandwidths of the two simple resonator cases are almost coincident as the resonance frequencies are identical, while the STL magnitudes are different because of different mass distribution, however, the STL differences are tiny as the mass differences of the resonators are not significant. Compared with simple resonator cases, the composite resonator A and B cases all show wider working bandwidth, without significant decrease in STL magnitudes. However, the bandwidth or STL magnitude is slightly different in the two composite resonator cases. In Fig.14, composite resonator B cases have larger STL magnitudes, but with narrower working bandwidth, and more drastic STL decreases beyond these resonance frequencies.

In a word, multiple simple resonator cases are applicable to simple STL modulation solutions, as both the bandwidths and magnitudes can be tuned as desired; however, if wider bandwidths are anticipated and a tradeoff in the magnitudes is acceptable, composite resonator cases can be the right alternatives.

4. Conclusions

By incorporating macroscopic locally resonant design (resonators) into composite structure with porous lining, we proposed an effective wideband acoustic abatement

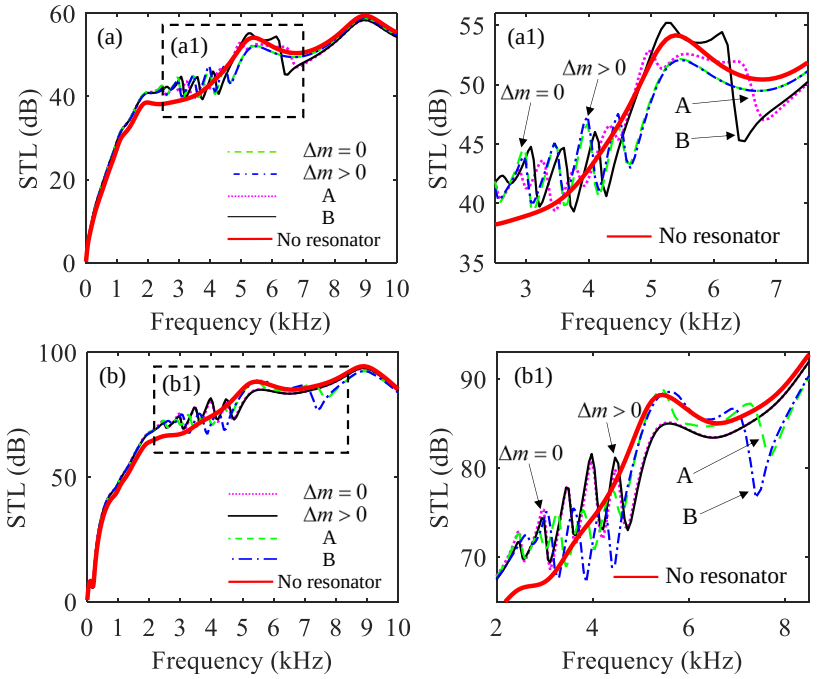

Fig. 14. Comparison of the four resonator cases (a-a1) OU case and (b-b1) UU case. $\Delta m = 0$ and $\Delta m > 0$ correspond to the multiple simple resonator cases I and II respectively. (a1) and (b1) shows the partial highlighted view of (a) and (b).

solution here, which is comprised of periodic resonators and multi-panel structures with porous lining.

We found that the STL of the periodic composite structure can be considered as the superposition of contributions from porous additions and resonators separately, therefore, it can be tuned using proper resonator arrangements concerning both the amplitude and the tuning bandwidth. When the resonance frequencies of the resonators are in the low-frequency range, notable STL improvements occur nearby, with a decrease around the subsequent anti-resonance frequencies (a local trough); however, as the resonance frequencies increase, the improvement nearby weakens. Meanwhile, the STL amplitude and its modulation bandwidth can be tuned by different resonator configurations. Compared to the simple resonator cases, composite resonator cases can obtain wider bandwidths while a tradeoff in the magnitudes is inevitable.

It is illustrated that the wideband capability of porous materials and low-frequency advantage of periodic structures can be utilized and incorporated together here. Though the results are preliminary here, this synergetic effect is exciting, and can be promising in the research on low-frequency wideband sound modulation.

Acknowledgements

This work is supported by the National Natural Science Foundation of China (NSFC) No.11572137.

Appendix A. The non-zero elements in matrices of composite resonators

The non-zero elements in matrices $\mathbf{K}, \mathbf{C}, \mathbf{M}$, and vector $\mathbf{F}$ of composite resonator A are

$$\begin{gathered}
K(1,1)=k_2^i,\ K(1,2)=-k_2^i,\ K(2,1)=-k_1^i-k_2^i \\
K(2,2)=k_2^i,\ K(3,1)=k_1^i,\ K(3,3)=-1 \\
C(1,1)=\zeta_2^i,\ C(1,2)=-\zeta_2^i,\ C(2,1)=-\zeta_1^i-\zeta_2^i \\
C(2,2)=\zeta_2^i,\ C(3,1)=\zeta_1^i \\
M(1,2)=-m_2^i,\ M(2,1)=-m_1^i \\
F(2)=-k_1^i-\mathrm{j}\omega\zeta_1^i,\ F(3)=k_1^i+\mathrm{j}\omega\zeta_1^i
\end{gathered} \tag{A.1}$$

The non-zero elements in matrices $\mathbf{K}, \mathbf{C}, \mathbf{M}$, and vector $\mathbf{F}$ of composite resonator B are

$$\begin{gathered}
K(1,1)=-k_1^i-\tfrac{k_2^i}{2},\ K(1,2)=\tfrac{k_2^i}{2},\ K(2,1)=\tfrac{k_2^i}{2} \\
K(2,2)=-k_2^i,\ K(3,1)=k_1^i,\ K(3,2)=\tfrac{k_2^i}{2},\ K(3,3)=-1 \\
C(1,1)=-\zeta_1^i-\tfrac{\zeta_2^i}{2},\ C(1,2)=\tfrac{\zeta_2^i}{2},\ C(2,1)=\tfrac{\zeta_2^i}{2} \\
C(2,2)=-\zeta_2^i,\ C(3,1)=\zeta_1^i,\ C(3,2)=\tfrac{\zeta_2^i}{2} \\
M(1,1)=-m_1^i,\ M(2,2)=-m_2^i \\
F(1)=-k_1^i-\mathrm{j}\omega\zeta_1^i,\ F(2)=-\tfrac{k_2^i}{2}-\mathrm{j}\omega\tfrac{\zeta_2^i}{2} \\
F(3)=k_1^i+\tfrac{k_2^i}{2}+\mathrm{j}\omega\zeta_1^i+\mathrm{j}\omega\tfrac{\zeta_2^i}{2}
\end{gathered} \tag{A.2}$$

Appendix B. The coefficient matrices of poroelastic variables

The non-zero elements of coefficient matrix $\mathbf{Y}_m$ are

$$\begin{gathered}
Y_m(1,1)=Y_m(1,2)=\tfrac{\mathrm{j}k_x^m}{k_1^2},\ Y_m(1,3)=Y_m(1,4)=\tfrac{\mathrm{j}k_x^m}{k_2^2} \\
Y_m(1,5)=\tfrac{\mathrm{j}k_{3z}^m}{k_3^2},\ Y_m(1,6)=-\tfrac{\mathrm{j}k_{3z}^m}{k_3^2} \\
Y_m(2,1)=\tfrac{\mathrm{j}k_{1z}^m}{k_1^2},\ Y_m(2,2)=-Y_m(2,1),\ Y_m(2,3)=\tfrac{\mathrm{j}k_{2z}^m}{k_2^2},\ Y_m(2,4)=-Y_m(2,3) \\
Y_m(2,5)=Y_m(2,6)=-\tfrac{\mathrm{j}k_x^m}{k_3^2} \\
Y_m(3,1)=Y_m(3,2)=b_1\tfrac{\mathrm{j}k_x^m}{k_1^2},\ Y_m(3,3)=Y_m(3,4)=b_2\tfrac{\mathrm{j}k_x^m}{k_2^2} \\
Y_m(3,5)=g\tfrac{\mathrm{j}k_{3z}^m}{k_3^2},\ Y_m(3,6)=-g\tfrac{\mathrm{j}k_{3z}^m}{k_3^2} \\
Y_m(4,1)=b_1\tfrac{\mathrm{j}k_{1z}^m}{k_1^2},\ Y_m(4,2)=-Y_m(4,1),\ Y_m(4,3)=b_2\tfrac{\mathrm{j}k_{2z}^m}{k_2^2},\ Y_m(4,4)=-Y_m(4,3) \\
Y_m(4,5)=Y_m(4,6)=-g\tfrac{\mathrm{j}k_x^m}{k_3^2}
\end{gathered}$$

Here, k_1, k_2, k_3, b_1, b_2, and g were detailed before in Ref. [7, 23].

Appendix C. The summation in Eq.(16).(x)

According to Eq.(6) and the Poisson summation formula [23]

$$\sum_m \delta(x - ml_x - x_i) = \frac{1}{l_x}\sum_m \mathrm{e}^{\mathrm{j}2\pi m(x-x_i)/l_x} \tag{C.1}$$

The summation

$$S = \sum_{i=0}^{N_s}\sum_m \beta_i F_i \delta(x - ml_x - x_i)$$

becomes

$$S = \frac{1}{l_x}\sum_{i=0}^{N_s} \frac{m_i\omega^2\beta_i}{1-\omega^2/[\omega_i^2(1+\mathrm{j}\eta_i)]} \sum_m\sum_n \mathrm{e}^{\mathrm{j}2\pi m(x-x_i)/l_x} W_n \mathrm{e}^{-\mathrm{j}k_x^n x} \tag{C.2}$$

In the meantime, there is an identity

$$\sum_n\sum_m W_m \mathrm{e}^{-\mathrm{j}k_x^m x}\mathrm{e}^{\mathrm{j}2\pi n(x-x_i)/l_x} = \sum_n W_n \mathrm{e}^{\mathrm{j}2\pi n(-x_i)/l_x}\sum_m \mathrm{e}^{-\mathrm{j}k_x^m x}\mathrm{e}^{\mathrm{j}2\pi(-m)(-x_i)/l_x} \tag{C.3}$$

where integer $m, n = -\infty, \ldots +\infty$; its derivation is provided in Appendix D. Accordingly, Eq.(C.2) becomes

$$S = \frac{1}{l_x}\sum_{i=0}^{N_s} \frac{m_i\omega^2\beta_i}{1-\omega^2/[\omega_i^2(1+\mathrm{j}\eta_i)]} \sum_n W_n \mathrm{e}^{\mathrm{j}2\pi n(-x_i)/l_x}\sum_m \mathrm{e}^{-\mathrm{j}k_x^m x}\mathrm{e}^{\mathrm{j}2\pi(-m)(-x_i)/l_x} \tag{C.4}$$

When the orthogonal property Eq.(17) is used, Eq.(C.4) becomes

$$\frac{1}{l_x}\int_{-l_x/2}^{l_x/2} S\mathrm{e}^{\mathrm{j}k_x^p x}\mathrm{d}x = \frac{1}{l_x}\sum_n W_n \mathrm{e}^{\mathrm{j}2\pi(n-p)(-x_i)/l_x}\sum_{i=0}^{N_s}\frac{m_i\omega^2\beta_i}{1-\omega^2/[\omega_i^2(1+\mathrm{j}\eta_i)]} \tag{C.5}$$

Equation (16) can then be rearranged into Eq.(18) utilizing Eq.(C.5).

Appendix D. Derivation of the double summation identity

As $\exp(-\mathrm{j}k_x^m x)\cdot\exp(\mathrm{j}2\pi nx/l_x) = \exp[-\mathrm{j}k_x^{(m-n)}x]$, the left-hand side of Eq.(C.3) becomes

$$\sum_{n=-\infty}^{+\infty}\left(\cdots + W_{-1}\,\mathrm{e}^{-\mathrm{j}k_x^{-1-n}x} + W_0\,\mathrm{e}^{-\mathrm{j}k_x^{-n}x} + W_1\,\mathrm{e}^{-\mathrm{j}k_x^{1-n}x} + \cdots\right)\mathrm{e}^{\mathrm{j}2\pi n(-x_i)/l_x} \tag{D.1}$$

As $n = -\infty, \ldots \infty$, if the index n loops over $(n-1)$ to $(n+1)$, Eq.(D.1) becomes

$$\begin{aligned}\Big\{\cdots &+ \left(\cdots + W_{-1}\,\mathrm{e}^{-\mathrm{j}k_x^{-n}x} + W_0\,\mathrm{e}^{-\mathrm{j}k_x^{-n+1}x} + W_1\,\mathrm{e}^{-\mathrm{j}k_x^{-n+2}x} + \cdots\right)\mathrm{e}^{\mathrm{j}2\pi(n-1)(-x_i)/l_x} + \\ &+ \left(\cdots + W_{-1}\,\mathrm{e}^{-\mathrm{j}k_x^{-n-1}x} + W_0\,\mathrm{e}^{-\mathrm{j}k_x^{-n}x} + W_1\,\mathrm{e}^{-\mathrm{j}k_x^{-n+1}x} + \cdots\right)\mathrm{e}^{\mathrm{j}2\pi(n+0)(-x_i)/l_x} + \\ &+ \left(\cdots + W_{-1}\,\mathrm{e}^{-\mathrm{j}k_x^{-n-2}x} + W_0\,\mathrm{e}^{-\mathrm{j}k_x^{-n-1}x} + W_1\,\mathrm{e}^{-\mathrm{j}k_x^{-n}x} + \cdots\right)\mathrm{e}^{\mathrm{j}2\pi(n+1)(-x_i)/l_x} + \cdots\Big\}\end{aligned} \tag{D.2}$$

If the terms with $\exp[-\mathrm{j}k_x^{-n-1}x]$, $\exp[-\mathrm{j}k_x^{-n}x]$, $\exp[-\mathrm{j}k_x^{-n+1}x]$...etc. in Eq.(D.2) were collected individually, Eq.(D.2) becomes

$$\begin{aligned}\Big\{ &\cdots + \mathrm{e}^{-\mathrm{j}k_x^{-n-1}x}\mathrm{e}^{-(-n-1)*}\left(\cdots + W_{-1}\mathrm{e}^{-1*} + W_0\mathrm{e}^{0*} + W_1\mathrm{e}^{1*} + \cdots\right) + \cdots \\ &+ \mathrm{e}^{-\mathrm{j}k_x^{-n}x}\mathrm{e}^{-(-n)*}\left(\cdots + W_{-1}\mathrm{e}^{-1*} + W_0\mathrm{e}^{0*} + W_1\mathrm{e}^{1*} + \cdots\right) + \cdots \\ &+ \mathrm{e}^{-\mathrm{j}k_x^{-n+1}x}\mathrm{e}^{-(-n+1)*}\left(\cdots + W_{-1}\mathrm{e}^{-1*} + W_0\mathrm{e}^{0*} + W_1\mathrm{e}^{1*} + \cdots\right) + \cdots \Big\}\end{aligned} \tag{D.3}$$

where $\mathrm{e}^{p*} = \mathrm{e}^{\mathrm{j}2\pi p(-x_i)/l_x}, p \in Z$. Subsequently, Eq.(D.3) becomes

$$\sum_n \sum_m W_m \mathrm{e}^{-\mathrm{j}k_x^m x}\mathrm{e}^{\mathrm{j}2\pi n(x-x_i)/l_x} = \sum_n W_n \mathrm{e}^{n*} \sum_m \mathrm{e}^{-\mathrm{j}k_x^m x}\mathrm{e}^{-m*} \tag{D.4}$$

Which is

$$\sum_n \sum_m W_m \mathrm{e}^{-\mathrm{j}k_x^m x}\mathrm{e}^{\mathrm{j}2\pi n(x-x_i)/l_x} = \sum_n W_n \mathrm{e}^{\mathrm{j}2\pi n(-x_i)/l_x} \sum_m \mathrm{e}^{-\mathrm{j}k_x^m x}\mathrm{e}^{\mathrm{j}2\pi(-m)(-x_i)/l_x} \tag{D.5}$$

Appendix E. The non-zero elements of the matrices in Eq.(18)

Denoting $k_x^m, k_{z,i}^m, k_{z,a}^m, k_{z,a}^m, k_{1z}^m, k_{2z}^m$, and k_{3z}^m as $\alpha_m, \gamma_{i,m}, \gamma_{a,m}, \gamma_{t,m}, \gamma_{1,m}, \gamma_{2,m}$, and $\gamma_{3,m}$ respectively; $L_1 = h_p + h_a$, $L_2 = h_p + h_a + \frac{h_1}{2}$, $L_3 = h_p + h_a + h_1$, the non-zero elements of matrix $\mathbf{A}_m$ are

$$A_m(1,1)=-Q_0-b_1R_0,\ A_m(1,2)=A_m(1,1),\ A_m(1,3)=-Q_0-b_2R_0$$
$$A_m(1,4)=A_m(1,3),\ A_m(1,8)=-\mathrm{j}\rho_i\epsilon\omega$$
$$A_m(2,1)=-A_0-b_1Q_0-2N_0\tfrac{\gamma_{1,m}^2}{k_1^2},\ A_m(2,2)=A_m(2,1)$$
$$A_m(2,3)=-A_0-b_2Q_0-2N_0\tfrac{\gamma_{2,m}^2}{k_2^2},\ A_m(2,4)=A_m(2,3)$$
$$A_m(2,5)=2N_0\alpha_m\tfrac{\gamma_{3,m}}{k_3^2},\ A_m(2,6)=-A_m(2,5),\ A_m(2,8)=-\mathrm{j}\rho_i(1-\epsilon)\omega$$
$$A_m(3,1)=-(1-\epsilon+b_1\epsilon)\tfrac{\gamma_{1,m}\omega}{k_1^2},\ A_m(3,2)=-A_m(3,1)$$
$$A_m(3,3)=-(1-\epsilon+b_2\epsilon)\tfrac{\gamma_{2,m}\omega}{k_2^2},\ A_m(3,4)=-A_m(3,3)$$
$$A_m(3,5)=(1-\epsilon+g\epsilon)\tfrac{\alpha_m\omega}{k_3^2},\ A_m(3,6)=A_m(3,5)$$
$$A_m(3,8)=\mathrm{j}\gamma_{i,m}$$
$$A_m(4,1)=2N_0\tfrac{\alpha_m\gamma_{1,m}}{k_1^2},\ A_m(4,2)=A_m(4,1),\ A_m(4,3)=2N_0\tfrac{\alpha_m\gamma_{2,m}}{k_2^2},\ A_m(4,4)=A_m(4,3)$$
$$A_m(4,5)=N_0\tfrac{-\alpha_m^2+\gamma_{3,m}^2}{k_3^2},\ A_m(4,6)=A_m(4,5)$$
$$A_m(5,1)=-(Q_0+b_1R_0)\mathrm{e}^{-\mathrm{j}h_p\gamma_{1,m}},\ A_m(5,2)=-(Q_0+b_1R_0)\mathrm{e}^{\mathrm{j}h_p\gamma_{1,m}}$$
$$A_m(5,3)=-(Q_0+b_2R_0)\mathrm{e}^{-\mathrm{j}h_p\gamma_{2,m}},\ A_m(5,4)=-(Q_0+b_2R_0)\mathrm{e}^{\mathrm{j}h_p\gamma_{2,m}}$$
$$A_m(5,9)=-\mathrm{j}\omega\epsilon\rho_a\mathrm{e}^{-\mathrm{j}h_p\gamma_{a,m}},\ A_m(5,10)=-\mathrm{j}\omega\epsilon\rho_a\mathrm{e}^{\mathrm{j}h_p\gamma_{a,m}}$$
$$A_m(6,1)=-(A_0+b_1Q_0+2N_0\tfrac{\gamma_{1,m}^2}{k_1^2})\mathrm{e}^{-\mathrm{j}h_p\gamma_{1,m}},\ A_m(6,2)=-(A_0+b_1Q_0+2N_0\tfrac{\gamma_{1,m}^2}{k_1^2})\mathrm{e}^{\mathrm{j}h_p\gamma_{1,m}}$$
$$A_m(6,3)=-(A_0+b_2Q_0+2N_0\tfrac{\gamma_{2,m}^2}{k_2^2})\mathrm{e}^{-\mathrm{j}h_p\gamma_{2,m}},\ A_m(6,4)=-(A_0+b_2Q_0+2N_0\tfrac{\gamma_{2,m}^2}{k_2^2})\mathrm{e}^{\mathrm{j}h_p\gamma_{2,m}}$$
$$A_m(6,5)=2N_0\tfrac{\alpha_m\gamma_{3,m}}{k_3^2}\mathrm{e}^{-\mathrm{j}h_p\gamma_{3,m}},\ A_m(6,6)=-2N_0\tfrac{\alpha_m\gamma_{3,m}}{k_3^2}\mathrm{e}^{\mathrm{j}h_p\gamma_{3,m}}$$
$$A_m(6,9)=-\mathrm{j}\omega(1-\epsilon)\rho_a\mathrm{e}^{-\mathrm{j}h_p\gamma_{a,m}},\ A_m(6,10)=-\mathrm{j}\omega(1-\epsilon)\rho_a\mathrm{e}^{\mathrm{j}h_p\gamma_{a,m}}$$
$$A_m(7,1)=-(1-\epsilon+b_1\epsilon)\tfrac{\gamma_{1,m}\omega}{k_1^2}\mathrm{e}^{-\mathrm{j}h_p\gamma_{1,m}},\ A_m(6,2)=(1-\epsilon+b_1\epsilon)\tfrac{\gamma_{1,m}\omega}{k_1^2}\mathrm{e}^{\mathrm{j}h_p\gamma_{1,m}}$$
$$A_m(7,3)=-(1-\epsilon+b_2\epsilon)\tfrac{\gamma_{2,m}\omega}{k_2^2}\mathrm{e}^{-\mathrm{j}h_p\gamma_{2,m}},\ A_m(7,4)=(1-\epsilon+b_2\epsilon)\tfrac{\gamma_{2,m}\omega}{k_2^2}\mathrm{e}^{\mathrm{j}h_p\gamma_{2,m}}$$
$$A_m(7,5)=(1-\epsilon+g\epsilon)\tfrac{\alpha_m\omega}{k_3^2}\mathrm{e}^{-\mathrm{j}h_p\gamma_{3,m}},\ A_m(7,6)=(1-\epsilon+g\epsilon)\tfrac{\alpha_m\omega}{k_3^2}\mathrm{e}^{\mathrm{j}h_p\gamma_{3,m}}$$
$$A_m(7,9)=-\mathrm{j}\gamma_{a,m}\mathrm{e}^{-\mathrm{j}h_p\gamma_{a,m}},\ A_m(7,10)=\mathrm{j}\gamma_{a,m}\mathrm{e}^{\mathrm{j}h_p\gamma_{a,m}}$$
$$A_m(8,1)=2N_0\tfrac{\alpha_m\gamma_{1,m}}{k_1^2}\mathrm{e}^{-\mathrm{j}h_p\gamma_{1,m}},\ A_m(8,2)=-2N_0\tfrac{\alpha_m\gamma_{1,m}}{k_1^2}\mathrm{e}^{\mathrm{j}h_p\gamma_{1,m}}$$
$$A_m(8,3)=2N_0\tfrac{\alpha_m\gamma_{2,m}}{k_2^2}\mathrm{e}^{-\mathrm{j}h_p\gamma_{2,m}},\ A_m(8,4)=-2N_0\tfrac{\alpha_m\gamma_{2,m}}{k_2^2}\mathrm{e}^{\mathrm{j}h_p\gamma_{2,m}}$$
$$A_m(8,5)=N_0\tfrac{-\alpha_m^2+\gamma_{3,m}^2}{k_3^2}\mathrm{e}^{-\mathrm{j}h_p\gamma_{3,m}},\ A_m(8,6)=N_0\tfrac{-\alpha_m^2+\gamma_{3,m}^2}{k_3^2}\mathrm{e}^{\mathrm{j}h_p\gamma_{3,m}}$$
$$A_m(9,7)=\mathrm{j}\omega,\ A_m(9,9)=-\mathrm{j}\gamma_{a,m}\mathrm{e}^{-\mathrm{j}L_1\gamma_{a,m}},\ A_m(9,10)=\mathrm{j}\gamma_{a,m}\mathrm{e}^{\mathrm{j}L_1\gamma_{a,m}}$$
$$A_m(10,7)=-D\alpha_m^4+\rho_p h_1\omega^2,\ A_m(10,9)=\mathrm{j}\omega\rho_a\mathrm{e}^{-\mathrm{j}L_2\gamma_{a,m}}$$
$$A_m(10,10)=\mathrm{j}\omega\rho_a\mathrm{e}^{\mathrm{j}L_2\gamma_{a,m}},\ A_m(10,11)=-\mathrm{j}\omega\rho_t\mathrm{e}^{-\mathrm{j}L_2\gamma_{t,m}}$$
$$A_m(11,7)=\mathrm{j}\omega,\ A_m(11,11)=-\mathrm{j}\gamma_{t,m}\mathrm{e}^{-\mathrm{j}L_3\gamma_{t,m}} \tag{E.1}$$

where $Q_0, R_0, A_0, N_0,\ k_1, k_2, k_3, b_1, b_2$, and g are detailed in Ref. [7, 23].

The non-zero elements of vector $\mathbf{p}$ are: $p(1)=\mathrm{j}\omega\epsilon\rho_i,\ p(2)=\mathrm{j}\omega(1-\epsilon)\rho_i,\ p(3)=\mathrm{j}k_z$.

The non-zero elements of matrix $\mathbf{B}_m$ in multiple simple resonator cases are provided here to illustrate the core ideas. Denoting the row and column block index of full block matrix $\tilde{\mathbf{B}}$ as m, n, if $N_s > 1$ and $m \neq n$, the non-zero element is

$$B_m(10,7) = -\frac{1}{l_x}\left[\sum_{i=1}^{N_s-1}\frac{k_i m_i \omega^2}{k_i - m_i\omega^2}\mathrm{e}^{\mathrm{j}2\pi(n-m)\frac{-ia}{l_x}} + \frac{1}{2}\frac{k_0 m_0 \omega^2}{k_0 - m_0\omega^2} + \frac{1}{2}\frac{k_{N_s} m_{N_s}\omega^2}{k_{N_s} - m_{N_s}\omega^2}\mathrm{e}^{\mathrm{j}2\pi(n-m)\frac{-N_s a}{l_x}}\right]$$

If $N_s > 1$ and $m = n$, the non-zero element is

$$B_m(10,7) = -\frac{1}{l_x}\left[\sum_{i=1}^{N_s-1}\frac{k_i m_i \omega^2}{k_i - m_i\omega^2} + \frac{1}{2}\frac{k_0 m_0 \omega^2}{k_0 - m_0\omega^2} + \frac{1}{2}\frac{k_{N_s} m_{N_s}\omega^2}{k_{N_s} - m_{N_s}\omega^2}\right]$$

If $N_s = 1$, the non-zero element is

$$B_m(10,7) = -\frac{1}{l_x}\frac{k_1 m_1 \omega^2}{k_1 - m_1\omega^2}$$

References

[1] M. A. Biot, Theory of propagation of elastic waves in a fluidsaturated porous solid. i. lowfrequency range, J Acoust Soc Am 28 (1956) 168–178.

[2] M. E. Delany, E. N. Bazley, Acoustical properties of fibrous absorbent materials, Appl Acoust 3 (1970) 105–116.

[3] J. Allard, Y. Champoux, New empirical equations for sound propagation in rigid frame fibrous materials, J Acoust Soc Am 91 (1992) 3346–3353.

[4] N. Atalla, R. Panneton, P. Debergue, A mixed displacement-pressure formulation for poroelastic materials, J Acoust Soc Am 104 (1998) 1444–1452.

[5] N. Atalla, M. A. Hamdi, R. Panneton, Enhanced weak integral formulation for the mixed (u,p) poroelastic equations, J Acoust Soc Am 109 (2001) 3065–3068.

[6] J. F. Allard, C. Depollier, P. Rebillard, W. Lauriks, A. Cops, Inhomogeneous Biot waves in layered media, J Appl Phys 66 (1989) 2278–2284.

[7] J. Bolton, N.-M. Shiau, Y. Kang, Sound transmission through multi-panel structures lined with elastic porous materials, J Sound Vib 191 (1996) 317 – 347.

[8] J. Zhou, A. Bhaskar, X. Zhang, Sound transmission through a double-panel construction lined with poroelastic material in the presence of mean flow, J Sound Vib 332 (2013) 3724 – 3734.

[9] R. Panneton, N. Atalla, Numerical prediction of sound transmission through finite multilayer systems with poroelastic materials, J Acoust Soc Am 100 (1996) 346–354.

[10] M. Lewińska, J. van Dommelen, V. Kouznetsova, M. Geers, Towards acoustic metafoams: The enhanced performance of a poroelastic material with local resonators, J Mech Phys Solids 124 (2019) 189–205.

[11] M. Lewińska, V. Kouznetsova, J. van Dommelen, M. Geers, Computational homogenisation of acoustic metafoams, Eur J Mech A Solids 77 (2019) 103805.

[12] Z. Liu, X. Zhang, Y. Mao, Y. Y. Zhu, Z. Yang, C. T. Chan, P. Sheng, Locally resonant sonic materials, Science 289 (2000) 1734–1736.

[13] Y. Xiao, J. Wen, X. Wen, Sound transmission loss of metamaterial-based thin plates with multiple subwavelength arrays of attached resonators, J Sound Vib 331 (2012) 5408–5423.

[14] H. Peng, P. Frank Pai, Acoustic metamaterial plates for elastic wave absorption and structural vibration suppression, Int J Mech Sci 89 (2014) 350–361.

[15] H. Peng, P. Frank Pai, H. Deng, Acoustic multi-stopband metamaterial plates design for broadband elastic wave absorption and vibration suppression, Int J Mech Sci 103 (2015) 104–114.

[16] H. Qiao, Z. He, H. Zhang, W. Peng, W. Jiang, Sound transmission in two-dimensional periodic poroelastic structures, Acta Phys Sin 68 (2019) 128101.

[17] F. Bucciarelli, G. Malfense Fierro, M. Meo, A multilayer microperforated panel prototype for broadband sound absorption at low frequencies, Appl Acoust 146 (2019) 134–144.

[18] H. Qiao, Z. He, C. Zhao, W. Jiang, W. Peng, Enhancing sound absorption using periodic micro-perforated structure with porous layer, Chinese J Acoust (2019) (In Press).
[19] N. Fang, D. Xi, J. Xu, M. Ambati, W. Srituravanich, C. Sun, X. Zhang, Ultrasonic metamaterials with negative modulus, Nat Mater 5 (2006) 452–456.
[20] A. Maurel, J.-F. Mercier, K. Pham, J.-J. Marigo, A. Ourir, Enhanced resonance of sparse arrays of Helmholtz resonatorsApplication to perfect absorption, J Acoust Soc Am 145 (2019) 2552–2560.
[21] X. Peng, J. Ji, Y. Jing, Composite honeycomb metasurface panel for broadband sound absorption, J Acoust Soc Am 144 (2018) EL255–EL261.
[22] H. Meng, M. Galland, M. Ichchou, F. Xin, T. Lu, On the low frequency acoustic properties of novel multifunctional honeycomb sandwich panels with micro-perforated faceplates, Appl Acoust 152 (2019) 31–40.
[23] H. Qiao, Z. He, W. Jiang, W. Peng, Sound transmission of periodic composite structure lined with porous core: Rib-stiffened double panel case, J Sound Vib 440 (2019) 256–276.
[24] J. F. Allard, N. Atalla, Propagation of Sound in Porous Media, John Wiley & Sons, Ltd, 2009.
[25] J. Legault, N. Atalla, Numerical and experimental investigation of the effect of structural links on the sound transmission of a lightweight double panel structure, J Sound Vib 324 (2009) 712–732.
[26] F. Xin, T. Lu, Analytical modeling of fluid loaded orthogonally rib-stiffened sandwich structures: Sound transmission, J Mech Phys Solids 58 (2010) 1374–1396.
[27] S. A. Hambric, S. H. Sung, D. J. Nefske, Engineering Vibroacoustic Analysis: Methods and Applications, John Wiley & Sons, 2016.